Available online at www.sciencedirect.com
ScienceDirect
Trans. Nonferrous Met. Soc. China 34(2024) 2800−2813
Transactions of Nonferrous Metals Society of China
www.tnmsc.cn

Twinning behaviors of Mg−Sn alloy with basal or prismatic Mg_2Sn

Rui-hao FU[1,2], Yang-jie WAN[2], Xun-fei XIONG[2], Dong-di YIN[2],
Man-ping LIU[3], Bin JIANG[1], Zi-rong ZHOU[4], Yu-yang GAO[1], Ying ZENG[1,2]

1. National Engineering Research Center for Magnesium Alloys, Chongqing University, Chongqing 400044, China;
2. Key Laboratory of Advanced Technologies of Materials, Ministry of Education,
School of Materials Science and Engineering, Southwest Jiaotong University, Chengdu 610031, China;
3. School of Materials Science and Engineering, Jiangsu University, Zhenjiang 212013, China;
4. Institute of Science and Technology Innovation, Dongguan University of Technology, Guangdong 523007, China

Received 31 March 2023; accepted 23 February 2024

Abstract: The Mg−Sn alloys, with basal or prismatic Mg_2Sn laths, were employed to reveal the effect of precipitate orientation on twinning behavior quantitatively. The Mg−5wt.%Sn alloys with basal or prismatic Mg_2Sn were compressed to study the twinning behaviors. Subsequently, an Orowan strengthening model was developed to quantitatively investigate the critical resolved shear stress (CRSS) increment of precipitates on twinning. The results revealed that the prismatic precipitates hindered the transfer and growth of tensile twins more effectively compared with the basal precipitates. The decreased proportion of tensile twins containing prismatic Mg_2Sn might be attributed to a larger CRSS increment for tensile twins compared with that for basal precipitates. The obvious decreased twinning transfer in the alloy with prismatic Mg_2Sn could be due to its higher geometrically necessary dislocation and enhanced CRSS of tensile twins. Notably, the prismatic precipitates have a better hindering effect on tensile twins during compression.

Key words: Mg−Sn alloy; orientation regulation; twinning behavior; Mg_2Sn lath; Orowan strengthening

1 Introduction

Mg−Sn alloys exhibit the potential for age strengthening, they have significant differences in the solubility limit of the primary precipitate (Mg_2Sn) with temperature [1]. In binary Mg−Sn alloys, it has been observed that the Mg_2Sn phase predominantly precipitates on the $(0001)_\alpha$ basal plane along the $\langle 1\bar{2}10\rangle_\alpha$ ($\langle a\rangle$) direction, forming basal precipitates characterized by a lath shape and trigonal distribution [2,3]. Despite the remarkable aging response of the Mg_2Sn phase and the presence of abundant Mg_2Sn in aged Mg−Sn alloys, the strength and hardness of alloy remain constrained. The limited strengthening effect of these basal precipitates on Mg alloys is attributed to their weak hindrance of basal slip, which is the predominant deformation mechanism in Mg [4].

In comparison to basal precipitates, the second phase precipitated on the prismatic plane (referred to prismatic precipitates) demonstrates a heightened potential for strengthening and enhancing the yield strength of the alloys [5−7]. Consequently, purposefully adjusting the distribution of the Mg_2Sn phase from the basal plane to the prismatic plane emerges as an effective approach to enhance the strengthening of Mg−Sn alloys. Over the decades, numerous studies have observed a change in the precipitated orientation of the Mg_2Sn phase in

Corresponding author: Ying ZENG, Tel: +86-18048580882, E-mail: clzy@swjtu.edu.cn;
Yu-yang GAO, Tel: +86-15754302916, E-mail: gaoyuyang@cqu.edu.cn
DOI: 10.1016/S1003-6326(24)66577-5

Mg−Sn alloys, transitioning from the basal plane to non-basal planes with the addition of Zn [8,9]. Mg_2Sn phases were identified on the prismatic plane or inclined at specific angles to the $(0001)_\alpha$ basal plane, resulting in a significantly enhanced aging hardening response. However, due to the unpredictable effect of inter-elemental interferences on the precipitation behavior, the large formation of non-basal or prismatic Mg_2Sn phases by alloy addition is still challenging.

Our recent work [10] obtained abundant prismatic lath-shaped Mg_2Sn phase in a binary Mg−5wt.%Sn alloy by a process of twinning, aging, and detwinning (namely TAD) [11]. After the transformation of precipitation orientation from the basal plane to the prismatic plane, the yield strength and ductility of this alloy were enhanced simultaneously. In particular, the compressive yield strength (CYS) was increased by 137%. It is known that the wrought Mg alloys have a strong basal texture and when this alloy compresses along the deformed direction, most *c* axis of grains undergoes tension, and $\{10\bar{1}2\}$ tensile twin is activated [12]. Therefore, the compressive yield strength of wrought Mg alloy is closely related to its twinning behaviors during the compressive process [13]. That is, the contribution of prismatic precipitates in Mg−Sn alloy to twinning behaviors during compression might determine the CYS improvement to some extent. FAN et al [14] proposed an analytical model and molecular dynamics and predicted that the prismatic $Mg_{17}Al_{12}$ plates had a stronger blocking effect on twin boundary (TB) (~37 MPa) than that of the basal plate (~29 MPa). ROBSON et al [15] stated that basal plate precipitates (e.g. $Mg_{17}Al_{12}$) might be better strengtheners against twin growth compared with *c*-axis rods (e.g. Mg−Zn phase). There exists controversy regarding the obstructive impact of basal and prismatic precipitates on twinning. Moreover, there is a dearth of experimental evidence substantiating the role of prismatic precipitates in impeding twinning, particularly within the same precipitation system.

In this study, we obtained two different plates containing only basal or prismatic precipitates. The purpose is to conduct a quantitative analysis of twinning behavior during compression in Mg−Sn alloys. Initially, the evolution of the microstructure during compression is considered, and the influence of varied precipitate types on the nucleation, growth, and interaction of twinning is explored. Additionally, a model has been developed to explain the hindering effect of precipitates on twins, and the interactions between precipitates (both basal and prismatic precipitates) and twins have also been analyzed quantitatively.

2 Experimental

The material in this study is an as-extruded Mg−5wt.%Sn alloy sheet with a strong basal texture. Subsequent to its extrusion, this sheet undergoes a twinning-aging-detwinning (TAD) process [11] to acquire the prismatic Mg_2Sn phase, distributed along the prismatic plane. Conversely, another sheet undergoes direct aging to obtain the basal Mg_2Sn phase. Before compression, the directly aged samples are referenced to as EA, while those subjected to the TAD process are labeled as EDT. Further detailed procedures regarding the TAD and direct aging methodologies refer to our previous study [10].

To compare the twinning behaviors of Mg−Sn alloys with prismatic and basal precipitates during compression, the alloy sheets were compressed at a speed of 0.48 mm/min along the extrusion direction (ED) at room temperature. An interrupted compression at a strain of 4% was applied to reserving enough initial twins in the studied alloys. The direct aging sample after 4% compression is called as C4A and that of the sample processed by TAD is denoted as C4DT. Cubic compressive samples (width of 5 mm and height of 7.5 mm) were employed for interrupted compression using Mechanical Testing & Simulation (MTS) precision universal tester (CMT5105) at room temperature with a strain rate of 1×10^{-3} s^{-1}.

The microstructure was characterized using the electron backscatter diffraction (EBSD) technique and transmission electron microscopy (TEM, JEOL JEM−2100F operating at 200 kV). Etching was carried out using a solution containing perchloric acid and alcohol with a volume ratio of 1:9 for EBSD characterization. Analysis of twinning behaviors, including nucleation, growth, and interaction, was conducted through EBSD data utilizing the HKL−Channel 5 software and the MTEX toolbox in MATLAB. For TEM observations, samples were polished through twin-jet electro-

polishing in a solution of 2 vol.% perchloric acid in ethanol at a temperature of −50 °C.

3 Results and discussion

3.1 Effect of prismatic precipitates on twinning behaviors in Mg−Sn alloys

Figure 1 presents the EBSD maps illustrating Mg−5Sn alloys with the basal and prismatic precipitates before and after undergoing a 4% compression. The pre-compression states of both alloys exhibit characteristic rolled basal textures in Mg alloys. Deformation twinning is easily caused during compression along the extrusion direction (ED) [16]. Following the 4% compression, a large number of twins appear in both alloys, with a predominant presence of $\{10\bar{1}2\}$ tension twins.

Statistically, the twin area fractions in C4A and

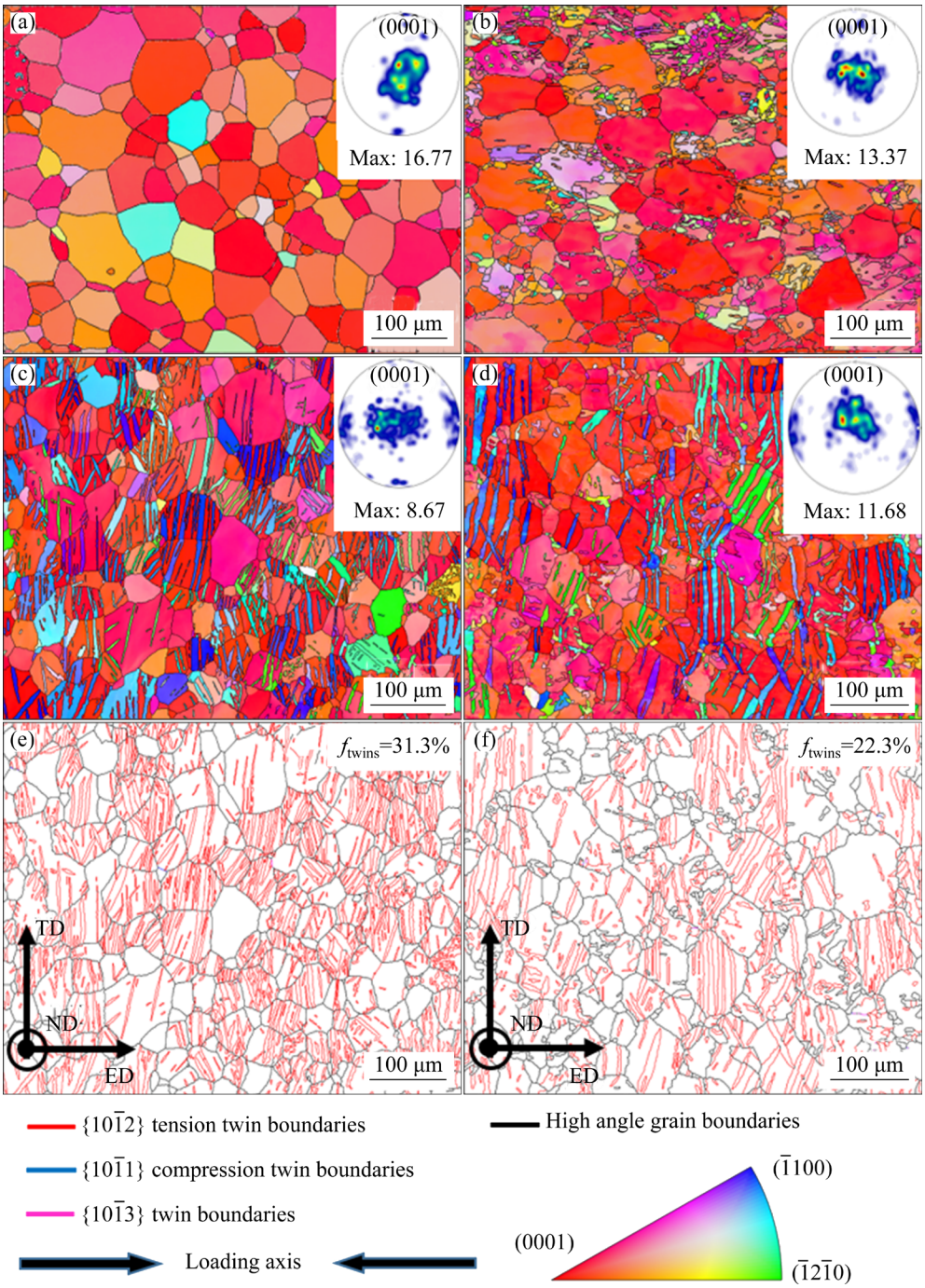

Fig. 1 EBSD inverse pole figure (IPF) maps of samples: (a, b) EA and EDT samples without deformation, respectively; (c, d) C4A and C4DT samples after 4% deformation, respectively; (e, f) High angle grain boundaries (HAGBs) and twin boundaries distribution map of C4A and C4DT samples, respectively (f_{twins}−Activated twin area fraction)

C4DT are 31.3% and 22.3%, respectively. Notably, the activated twin area fraction in C4DT is significantly lower than that in C4A under the same deformation conditions. The twin layers in C4A grains exhibit a generally uniform distribution, and the distribution of these grains where twinning occurs is more concentrated. Furthermore, a single grain in C4A may contain multiple twin variants, occupying a larger area. In C4DT, the other variants occupy a small area, and they exclude the variant with the most prominent activation area. Among them, many twin crossover (intersection of twin layers within a grain) and twinning transfers (or so-called paired twinning, interaction of twin layers at adjacent grain boundary (GB) or twins nucleate at the same location on the GB and grow into their respective parent grains) occur. To further quantitatively study the effect of prismatic precipitates on the twinning behavior of Mg−Sn alloy, the twins' variants, transfer, and crossover along with their nucleation, and growth are analyzed in detail.

The $\{10\bar{1}2\}$ twin model corresponds to six possible twin variants due to the particular hexagonal close-packed (HCP) structure of the Mg alloy [17]. Each twin variant was confirmed using superimposed polar plots [18] of the {0001} and $\{10\bar{1}2\}$ planes collected by EBSD. The detected plane of EBSD is the ED−TD plane. Figure 2 shows the variant identification of grains of activated twins in Samples C4A and C4DT. Normalized geometrical compatibility factor (m') was used to analyze the twinning transfer in adjacent grains. The normalized Schmid factor (SF) was used to explain the crossover behavior of twin variants, nucleation, and growth [19,20]. The normalized SF can be calculated by normalized $SF=(SF-SF_{min})/[2(SF_{max}-SF_{min})]$ [21], where SF is the value calculated directly for the system, and SF_{max} and SF_{min} are the maximum and minimum values of SF in the grain for all systems, respectively.

Based on statistical analysis using the MTEX toolbox in MATLAB [22], a total of 317 instances of twinning transfer were identified in 280 grain pairs in C4A, whereas only 104 twinning transfers were observed in 92 grains in C4DT. The number of twin-transfer chains in C4A was approximately three times that of C4DT. The twinning transfer is closely related to the misorientation of the adjacent

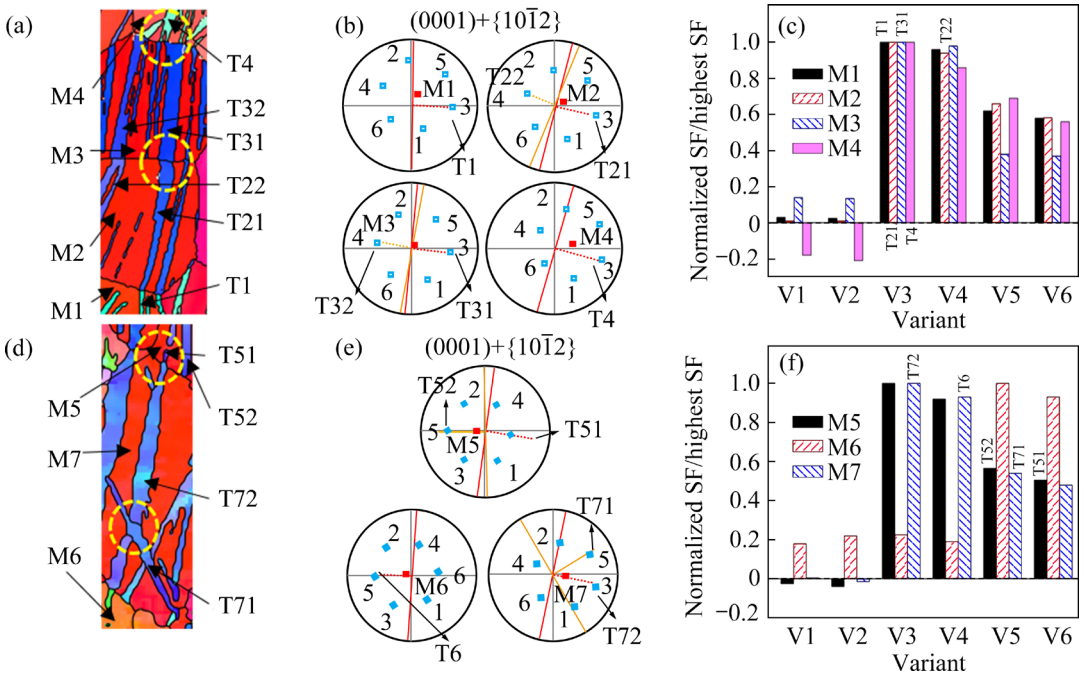

Fig. 2 (a, d) Partial EBSD maps of C4A sample and C4DT sample obtained on TD−RD plane, respectively (M represents grain of matrixes, T represents activated $\{10\bar{1}2\}$ twin variants; (b, e) Superposed {0001} (red point) and $\{10\bar{1}2\}$ (blue point) pole figures of grains in (a) and (d), respectively (The yellow and red lines are twin plane traces of corresponding variants); (c, f) Normalized SF of twin variants of parent grains in (a) and (d), respectively (V1−V6 denote six possible variants in the grain)

grains [22]. Analyzing the IPF diagrams in Fig. 2 for Samples C4A and C4DT reveals the formation of twin chains in both samples. Multiple twins exhibit effective overlap at grain boundaries and extend into the grains, suggesting the occurrence of twinning transfer. The normalized m' can be applied to measuring the two systems' geometrical compatibility and m' was counted for all grains where twinning transfer has occurred and then normalized by m' [19,23]. Compared with C4A, the m' of individual adjacent grains in C4DT is generally lower. Because C4DT undergoes additional deformation by the TAD process, more dislocations and grain misorientation exist. Strong textures are favorable conditions for the formation of twinning transfers in adjacent grains. The intense texture leads to at least one pair of huge normalized SF variants in each grain and high matching of high normalized SF variants in adjacent grains, making it easier for twinning transfer.

In addition, Figs. 2(d, e) show two pairs of double chains (T22-T32, T21-T31) in the parent crystals M2 and M3. Considering the initial texture of the sample, T21 and T22 are indexed to be different $\{10\bar{1}2\}$ twin variants formed in the same parent grain M2. The two pairs of variants are adjacent to each other on the {0001} and $\{10\bar{1}2\}$ superposition diagrams (Fig. 2(b)). Their orientations are close to each other, experiencing minimal hindrance during the process of twinning transfer at the interface. The misorientation of adjacent interfaces emerges as a crucial factor in affecting the twinning transfer. Samples containing prismatic precipitates undergoing additional deformation (TAD) have a greater misorientation and are less susceptible to twinning transfer. The crossover behavior of twin variants is closely related to the nucleation and growth of twins [24]. In Figs. 2(a, d), the yellow circles indicate the areas of twinning crossover and transfer. The preference for twin variants within individual grains in C4A and C4DT predominantly adheres to the general Schmid's law, indicating that the vast majority of variants with large SF are preferentially activated within the grain. The normalized SF statistics of the twin variants are presented in Figs. 2(c, f). Within the grain, the variant with the maximum number of activations and the largest area of twinning regions consistently exhibits a high normalized SF. The number and area share of twin activation can be used to replace the nucleation rate and twin growth rate [23], and variants with a more prominent normalized SF indicate high nucleation rate and twin growth rate. In Figs. 2(d−f), the twin variant T72 has the most significant normalized SF in this grain, along with the largest number and area of activation, implying its preferential activation. This is evident in the presence of multiple twin layers running parallel to it throughout the grain. Similarly, T71 intersects with T72 but is obstructed by another T72, indicating its subsequent activation. As a result, T71 presents thin and continuous bands with a relatively small proportion of twin area. Misorientation in grain between the upper and lower regions of the parent grain reveals local strain inhomogeneity. The activation of the T71 twin may be intended to coordinate the deformation of the other twins within the grain to accommodate the external strain.

Therefore, as shown in Figs. 2(a, d), most of the twins nucleate at the grain boundaries and expand into the grains, which can be attributed to the stress concentration at grain boundaries induced by macroscopic stress [25,26]. Adjacent grains preferentially twin at grain boundaries to nucleate to reduce stress concentration [27]. Nevertheless, it is not clear why the orientation of the precipitates makes the twin nucleation growth of C4A higher than that of C4DT. This will be given in the results of the subsequent model analysis after the analysis of the twin.

The statistical analysis of the normalized SF of all grains shows that the normalized SF of most twins is significantly greater than 0.6. It is found that the twins preferentially activate the variants with high SF, which is consistent with the results of the local area analysis of the variants. However, in some grains, the SF of the twin variant is not the largest (Fig. 3(a)). This variant has the maximum number of activations and the maximum area in the grain, commonly referred non-Schmid twinning [28−30]. Many other external conditions also influence the activation and growth of twin crystals. Due to the special HCP structure of Mg alloys, when the grains are compressed along the vertical *c*-axis, the SF of the activated variants varies considerably with the compression angle [31]. XU et al [32] stated that the alloy was deformed unevenly during the deformation process and proposed

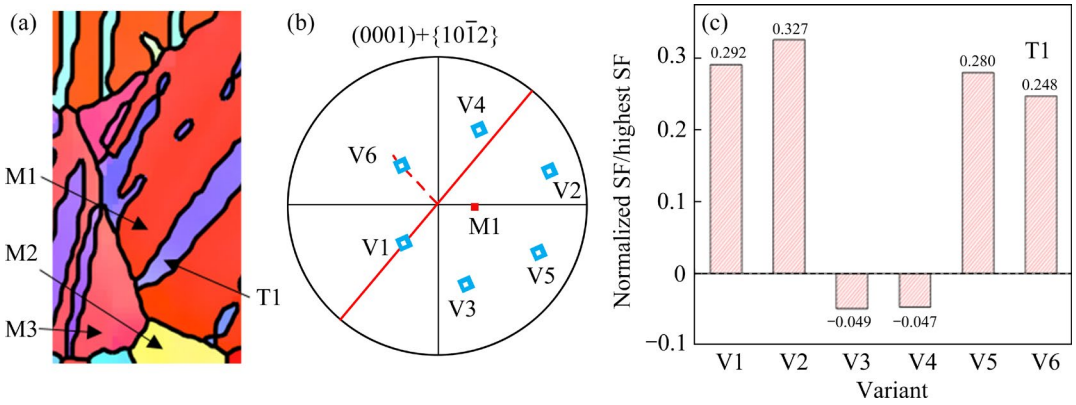

Fig. 3 (a) Partial EBSD map of non-Schmid twins in C4A sample; (b) Superposed {0001} (red point) and {10$\bar{1}$2} (blue point) pole figure of parent grain M1 (The red lines are twin plane traces of the corresponding variants); (c) SF distribution of variants of T1 twin in M1 grain

that there was a kind of back-stress in this process. The grains are unevenly stressed due to local deformation, and the grains apply additional local stress to the neighboring grains. In Fig. 3(c), although the SF of T1 is not the largest (the fourth one), its appearance is not accidental. T1 nucleates grows in the left lower section of the M1 grain. The IPF shows a significant color difference between the upper and lower part of the M2 grain, with a significant grain misalignment. The macroscopic stress direction is horizontal, but the lower left grain (M2, M3) will likely provide a reaction force to M1. The stress concentration at the boundary between the M1 and M2 grains exerts additional stress on the interior of the M1 grain. The actual local stress direction in the lower left region of M1 deviates from the macroscopic stress, so the actual local SF of T1 should be larger than the macroscopic SF. Combined with the connection between the magnitude of the SF and the stress [31], the local SF corresponding to the variant of T1 is probably the most prominent local SF. The nucleation growth of the twin variant occurs at this time. This might be the reason that the T1 variant has the largest area. The non-Schmid twins are consistent with the SF law after local stress analysis.

To further evaluate the influence of precipitate orientations on the twin behaviors, the SF rank and normalized SF distribution of all activated twins in Samples C4A and C4DT are presented in Fig. 4, where f_{R1+R2} and $f_{Nor.SF>0.6}$ denote the fraction of activated twins in the top two of the SF rank and activated twins with normalized SF more than 0.6, respectively. 75% of the activated twins in Sample C4A have SF ranking 1 and 2. The normalized SF distribution shows that 93% of all activated twins in Sample C4A have the normalized SF which is greater than 0.6 (Figs. 4(a, b)), and the selection of these twin variants follows the Schmid's law. In Sample C4DT, 76% of the activated twins have SF distribution at SF ranking 1 and 2; 94% of all activated twins have normalized SF greater than 0.6 (Figs. 4(c, d)). Combined with the above analysis of the transfer and crossover behavior of the variants, the selection of variants in samples C4A and C4DT conforms to the Schmid's law. Moreover, there are evident differences in twinning transfer, twin nucleation, and growth efficiency.

Figure 5(a) shows the statistical results of the twin boundary fraction and twin area fraction in Samples C4A and C4DT. It can be seen that the twin boundary fraction and twin area fraction of Sample C4A are 43.3% and 31.3%, respectively, which are higher than those of Sample C4DT (20.2% and 22.3%). The number of {10$\bar{1}$2} twin lamellae per grain (L_G) is related to the rate of twin nucleation. The area per {10$\bar{1}$2} twin lamella (A_L) is related to the rate of twin growth [33]. The statistical results for L_G and A_L are given in Figs. 5(b, c). According to the statistical results, the L_G in Sample C4DT is 2.4, which is lower than that in Sample C4A (3.6), indicating that the nucleation rate of twins in Sample C4DT might be lower than that in Sample C4A. On the other hand, the A_L in Sample C4DT is 596 μm^2, which is slightly lower than that of sample C4A (606 μm^2), demonstrating that the growth rate of twins in Sample C4DT might be also slightly lower than that in Sample C4A. The nucleation and growth rates of twins in Sample C4DT are lower than those in Sample C4A. However,

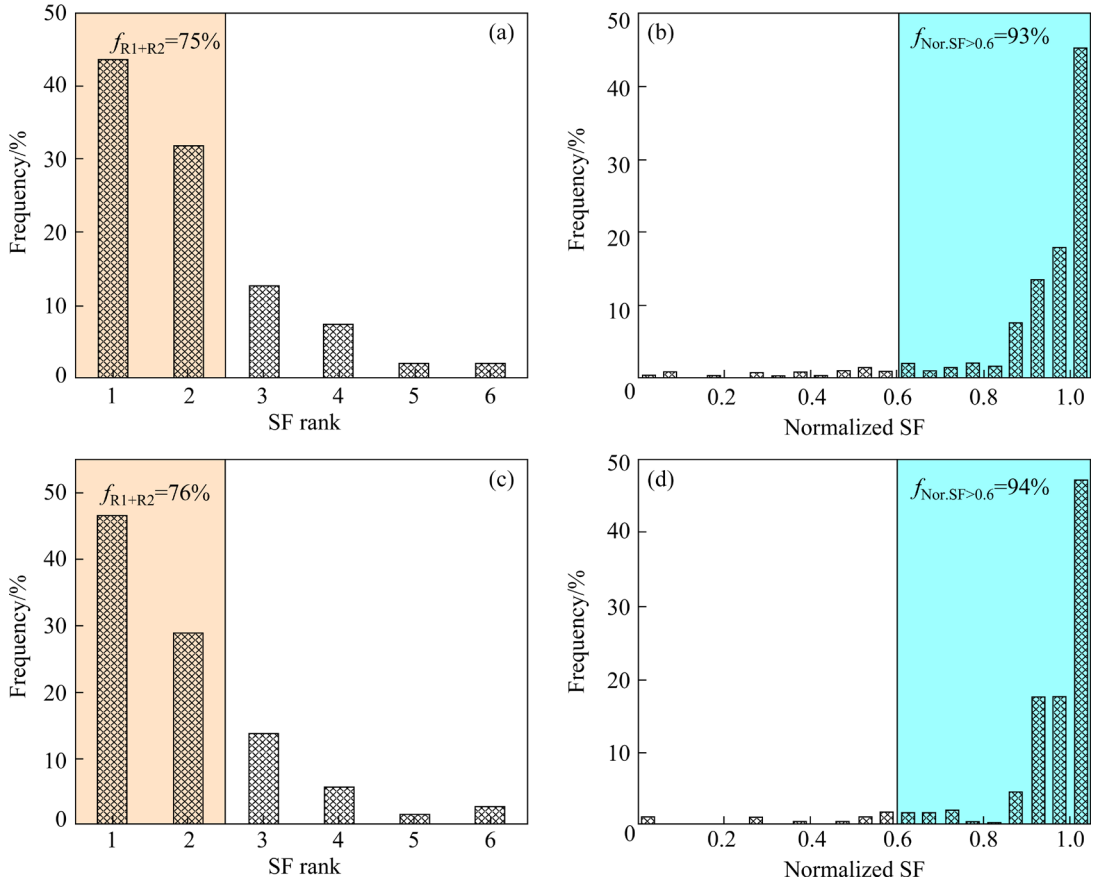

Fig. 4 Distribution of SF rank and normalized SF for activated twins in C4A sample (a, b) and C4DT sample (c, d)

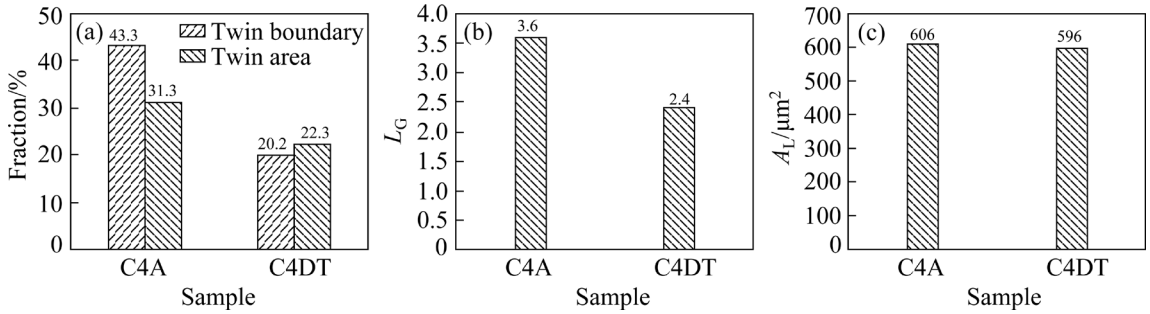

Fig. 5 Fraction of twin boundary and twin area (a), number of twin layers (b), and average area of twin layers (c)

the above results are not sufficient to prove that the prismatic Mg_2Sn phase can hinder both nucleation and growth of twins compared with the basal Mg_2Sn phase.

Figures 6(a, b) present the geometrically necessary dislocations (GND) in Samples C4A and C4DT. The value of GND is 6.05×10^{13} for Sample C4DT, while it is 4.67×10^{12} for Sample C4A. Sample C4DT has a larger GND than that of Sample C4A. The reason for the difference in twinning behavior could be caused by dislocations of different orders of magnitude within the material [34,35]. Therefore, the effect of dislocations on the twinning behaviors in C4A and C4DT alloys should be also considered. The difference in the twinning transfer can be attributed to the difference in GND, as the twinning transfer is closely related to the misorientation in the grain. Sample C4DT has a larger GND, the twinning transfer is more impeded, and the number of twinning transfers is much smaller than that in C4A, only 1/3 of C4A. Whether the modulated prismatic precipitates have a great hindering effect on the nucleation and growth of the twins relative to the basal precipitates needs to be measured quantitatively.

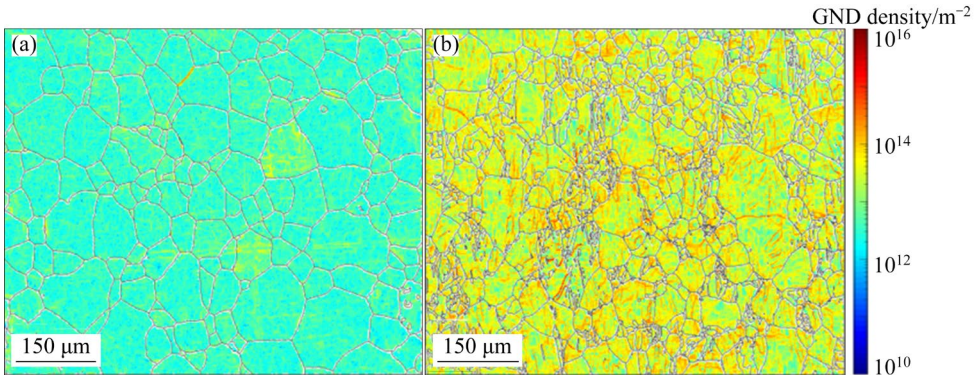

Fig. 6 Geometric necessary dislocation of C4A (a) and C4DT (b) samples

3.2 Quantified hindering model of prismatic precipitates with respect to twin

To quantify the hindering effect of the prismatic precipitates on the twin, a specific model calculation is required. NIE et al [5] and WANG et al [36] proposed the corresponding Orowan model assuming that the precipitates are arranged on the slip surface in a triangular manner to simplify the calculation model. ROBSON [37−39] and FULLMAN [40] considered the actual intersection of multiple distributions of the precipitates and proposed another modified Orowan model. The precipitates are regularly distributed on the slip surface with the intersection region of the slip surface. HIDALGO-MANRIQUE et al [41] also calculated the slatted precipitate parallel to the *c*-axis assuming a triangular arrangement of the precipitations relative to basal slip, prismatic slip, pyramidal $\langle c+a\rangle$ slip, and $\{10\bar{1}2\}$ tension twins for the critically resolved shear stress (CRSS) increments. Based on the model of HIDALGO-MANRIQUE [41], the CRSS increments of the prismatic and basal precipitates relative to the $\{10\bar{1}2\}$ tension twin are modeled to quantify the hindering effect. For the precipitates based on the bypass mechanism, the increment in CRSS (τ) is expressed as [5,42]

$$\Delta\tau=\frac{Gb}{2\pi\sqrt{1-\upsilon}}\left(\frac{1}{\lambda}\right)\ln\frac{\delta}{r_0} \tag{1}$$

where G is the shear modulus of the Mg matrix (16.5 GPa), b is the amplitude of the Burgers vector for the gliding dislocations in Mg, υ is the Poisson's ratio of the Mg matrix (0.35), δ is the mean planar diameter of the particles on the twin plane, λ is the effective planar interparticle spacing on the twin plane, which is based on the premise of an ideal distribution of the precipitates on the basal and prismatic plane [39], and r_0 is the core radius of the dislocations in Mg. The magnitude of b is equal to $a/7$ for twinning dislocations [43]. r_0 is the area around the dislocated, and it is generally thought to be $r_0=b$. However, based on the calculated study [44,45], $r_0=3a$ was taken from the twins. Notably, b of twins is one order of magnitude smaller than that of the slip dislocated. In Table 1 the calculated specific values of b and r_0 are given.

Table 1 Amplitude of burgers vector (b) and dislocation core radius (r_0) for calculation of Orowan stresses [41]

Dislocation	b/Å	r_0/Å
Basal $\langle a\rangle$	3.2	3.2
Twinning	0.458	9.6

In Formula (1), δ is also the effective obstruction length of the precipitated phase in the direction of twinning motion in the twinning plane. As shown in Figs. 7(b, e), since the precipitated phase is trigonal in the basal plane, the calculation of δ is divided into δ_x (x=1, 2, 3). Due to the different dislocations in the twin plane, the prismatic phase is subdivided into six cases (x=1, 2, 3, 4, 5, 6). The value of δ is a combination of the values taken for δ_x. The δ_x is calculated from the angle given in Figs. 7(b, e). The result is

$$\delta^{\text{basal}}=\frac{1}{3}\left(\frac{1}{3}\delta_1+\frac{2}{3}\delta_{2/3}\right)=0.1111l+0.2566w+0.1629t \tag{2}$$

$$\delta^{\text{prismatic}}=\frac{1}{3}\left[\frac{2}{3}(\delta_1+\delta_2+\delta_3)+\frac{1}{3}(\delta_4+2\delta_{5/6})\right]=0.2228l+0.6283w+0.3939t \tag{3}$$

where l, w and t are the length, width and thickness of the precipitates, respectively.

The average size of the projection spacing of the precipitates on the twin plane in the basal or prismatic plane can be obtained by the following equation [5]:

$$\lambda=\frac{1}{\sqrt{N_{\mathrm{A}}}}-\delta \tag{4}$$

where N_{A} is the number of phases per unit area on the slip plane, and its calculation formula is as follows [38]:

$$N_{\mathrm{A}}=\frac{f_{\mathrm{v}}}{S_{\mathrm{p}}} \tag{5}$$

where f_{v} is the volume fraction of precipitate; S_{p} is the average intersection area of the precipitate and the twin plane. The precipitates of different orientations are different from the intersection area of the twin planes. Similar to δ, the calculation of S_{p} is divided into various cases depending on the orientation of the precipitated phase. Here, $S_{\mathrm{p}x}$ (x=1−6) is calculated when the area of the intersection surface in Figs. 7(b, e) is related to the dimensions of the precipitated phase (l, w, t). The angle of each intersection surface is indicated in the figure. Figure 7(b) shows the intersection area of the basal precipitates and the twin plane. It can be seen that there are two situations in the intersection area of them, and the area of the intersection area is shown in Fig. 7(c). The calculation is as follows:

$$S_{\mathrm{p}}^{\mathrm{basal}}=\frac{1}{3}S_{\mathrm{p1}}+\frac{2}{3}S_{\mathrm{p2}}=$$
$$0.4888lt+1.1287wt \tag{6}$$

Figure 7(e) shows the intersection area of the prismatic precipitates and the twin plane. It can be seen that there are five situations in the intersection area of them, and the area of the intersection area is shown in Fig. 7(f). The calculation is as follows:

$$S_{\mathrm{p}}^{\mathrm{prismatic}}=\frac{1}{3}\left[\frac{2}{3}\left(S_{\mathrm{p1}}+S_{\mathrm{p2}}+S_{\mathrm{p3}}\right)+\frac{1}{3}\left(S_{\mathrm{p4}}+2S_{\mathrm{p5/6}}\right)\right]=$$
$$0.3897lw+0.9021wt \tag{7}$$

Substituting Eqs. (2)−(7) into Eq. (1), the increments of CRSS relative to the twin obstruction of the basal and the prismatic precipitates are obtained, respectively:

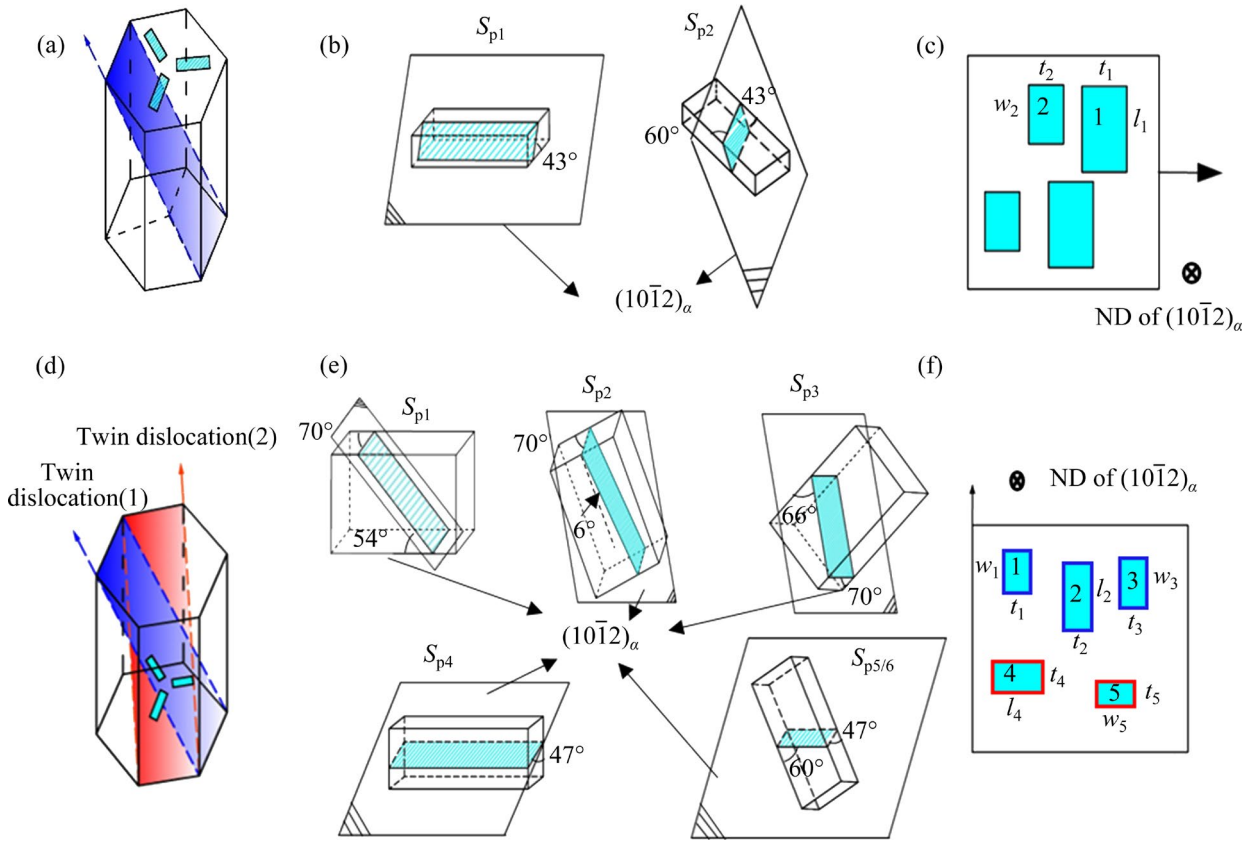

Fig. 7 Schematic views of basal or prismatic precipitates: (a, d) Positions of precipitates and tensile twin; (b, e) Intersection area of precipitates and twin plane; (c, f) Arrangement of precipitates in $(10\bar{1}2)$ twin plane

$$\Delta\tau_{\text{basal}}=149.18\sqrt{f_{\text{v}}}/[\sqrt{0.4888lt+1.1287wt}-(0.1111l+0.2566w+0.1629t)\sqrt{f_{\text{v}}}]\cdot\ln\frac{0.1111l+0.2566w+0.1629t}{9.6} \quad (8)$$

$$\Delta\tau_{\text{prismatic}}=149.18\sqrt{f_{\text{v}}}/[\sqrt{0.3897lw+0.9021wt}-(0.2228l+0.6283w+0.3939t)\sqrt{f_{\text{v}}}]\cdot\ln\frac{0.2228l+0.6283w+0.3939t}{9.6} \quad (9)$$

The above calculation formulas show that the increment of the CRSS of the twin is related to the size (l, w, t) of precipitates and their volume fraction (f_{v}). Then, the orientation of the precipitates in the EA and EDT samples is verified by TEM, and the size and prismatic fraction of the precipitates are calculated.

Figure 8(a) shows the morphology of the precipitates observed along the $[0001]_\alpha$ zone axis of the Sample EA. It can be seen that most of the lath-like Mg_2Sn phases are distributed along $\langle 11\bar{2}0\rangle_\alpha$, and a few of them are distributed along $\langle 10\bar{1}0\rangle_\alpha$ When viewed along the $[0001]_\alpha$ zone axis in Fig. 8(b), the direction of the basal precipitates is consistent and the length is different. Figure 8(c) illustrates two Mg_2Sn phases observed along the $[0001]_\alpha$ zone axis at high magnification. The angle between the long axis of the Mg_2Sn phase and the $(1\bar{1}00)_\alpha$ plane is about 3.6°, which may be caused by the interaction between twinning and precipitate. Figure 8(c) indicates the direction of deviation. When observed along the $[10\bar{1}0]_\alpha$ (Fig. 8(d)) zone axis, the precipitates are again distributed in a "herringbone" shape, and the long axis of some Mg_2Sn phases are parallel to the $[1\bar{2}10]_\alpha$. Almost all Mg_2Sn phases in the Sample EDT are indeed distributed parallel to the prismatic under the control of the TAD method.

The statistical results of the average size (l, w, and t), f_{v} and number per unit volume (N_{v}) of the precipitates in Samples EA and EDT can be found in our previous study [10]. For the lath-like Mg_2Sn phase distributed on the basal plane in Sample EA, the length refers to the dimension along the long axis of the lath-like Mg_2Sn observed along the $[0001]_\alpha$ zone axis. The dimension perpendicular to the long axis is the width. The thickness refers to the dimension of the short side of the lath as observed along the $[11\bar{2}0]_\alpha$ axis. As for the prismatic precipitates in Sample EDT, when the zone axis is perpendicular to the c-axis (along $[10\bar{1}0]_\alpha$), as shown in Fig. 8(d), the length and width refer to the dimensions observed directly. When the zone axis is parallel to the c-axis (along $[0001]_\alpha$), as shown in Fig. 8(c), the thickness (t) refers to the short side of the precipitates observed. The morphology of the precipitated phase does not change after modulation to the prismatic plane. The average size of the precipitates is derived from the average of more than 500 precipitates. The f_{v} statistical method of precipitates is $f_{\text{v}}=nV_{\text{p}}/(Ah)$ [41], where n is the number of precipitates in the statistical region, V_{p} ($V_{\text{p}}=lwt$) is the average volume of precipitates, A is the area of the statistical area, h is the thickness of the statistical region, and f_{v} and N_{v} are the averages of the statistical results of different regions from five TEM images.

In Sample EDT, the average dimensions of the Mg_2Sn phase are recorded as 1140 nm in length, 173 nm in width, and 93 nm in thickness. This sample exhibits a reduced size of the Mg_2Sn phase compared with Sample EA, where the average dimensions measured were 1262 nm in length, 188 nm in width, and 100 nm in thickness. The f_{v} and N_{v} of the precipitates in the Sample EDT are 4.9% and $3.3\times10^{18}/\text{m}^3$, respectively, which are also higher than those of the Sample EA (4.1% and $2.1\times10^{18}/\text{m}^3$). This may be attributed to that the twins and dislocations introduced by pre-compression provide more nucleation sites for Mg_2Sn, which promotes the precipitation of the Mg_2Sn phase [34,46,47].

The data of the average size, f_{v} and N_{v} are substituted into Eqs. (8) and (9) to obtain the CRSS increments ($\Delta\tau$) of the basal and prismatic precipitates relative to the twin obstruction.

The results reveal that the increment of CRSS of basal precipitates relative to the twin is 0.357, which is slightly smaller than that of prismatic precipitates relative to the twin of 0.5756. Assuming a constant size of the precipitates, the volume fraction of the precipitates for both orientations of the plates gradually becomes larger if aging is continued until the peak, as shown in Fig. 9(a). The $\Delta\tau$ of prismatic precipitates increases as the volume fraction increases significantly larger than that of the basal precipitates. The larger amount and the larger volume fraction of

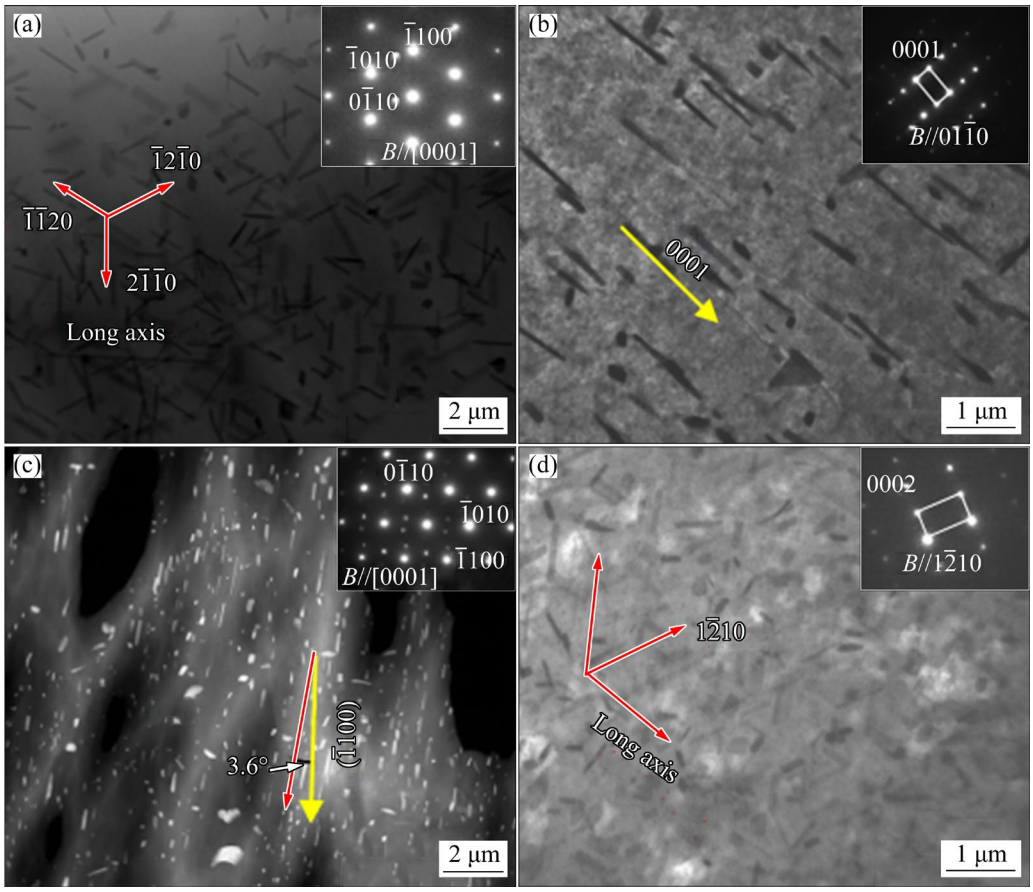

Fig. 8 TEM images of Samples *A* (a, b) and TAD (c, d) (The red arrows indicate the distribution direction of the long axis of the precipitates. The yellow arrows indicate the corresponding planes. The diffraction pattern is given in the upper right corner)

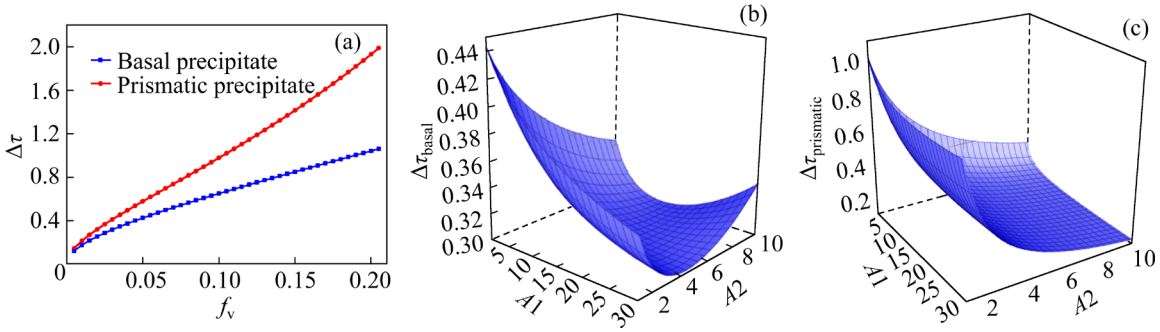

Fig. 9 Folding line chart of $\Delta\tau$ versus volume fraction f_v (a), and three-dimensional surface maps of $\Delta\tau$ with size of basal (b) and prismatic (c) precipitates

precipitates will result in the larger $\Delta\tau$, indicating that precipitates do have a hindering effect on twinning. The hindering effect of basal precipitates on twinning is smaller than that of prismatic precipitates, which is consistent with our observations. The twinning area in Sample C4A is larger than that in Sample C4DT. Sample C4A is more prone to twinning and possesses greater nucleation rates and growth rates.

The model data are further processed by defining the aspect ratio of the precipitate as $A1$ ($A1=l/w$) and the aspect ratio as $A2$ ($A2=w/t$), which results in an aspect ratio of $A1A2$ ($A1A2=l/t$). Figures 9(b, c) show the variation of CRSS increment for two oriented precipitates at different $A1$ and $A2$ for a certain volume fraction. The CRSS increment is the largest when both $A1$ and $A2$ tend to be 1, indicating that the more the shape of the

precipitates tends to be square, the stronger the hindering effect on twinning. In Fig. 9(b), when the $A2$ of the basal precipitates is about 4, the smaller $A1$ will lead to the least hindering effect on twinning. In Fig. 9(c), with the increases of $A1$ and $A2$, the hindering effect of the column surface relative to twinning gradually decreases, where the change of $A2$ has a great effect on the hindering effect.

A larger CRSS increment for a certain deformed mode always indicates a greater effect on the hindering effect and harder further deformation. Thus, according to the above calculated result, the decreased proportion of tension twins in Mg−Sn alloy containing prismatic Mg_2Sn illustrated in Fig. 1 might be attributed to the larger CRSS increment for tensile twin compared with the basal precipitates. In addition to the decrease in the area fraction of tension twins, compared with the alloy containing prismatic precipitates and that with basal ones, the amount of twinning transfer decreases shapely from 317 to 104. This obviously decreased twinning transfer in Mg−Sn alloy containing prismatic Mg_2Sn could be due to two factors. One is the higher geometry necessary dislocation in the alloy with prismatic precipitates, which hindered the transfer of tensile twin. The other is that the prismatic precipitates enhanced the CRSS of the tensile twin and thereby impeded its transfer.

4 Conclusions

(1) The Mg−Sn alloy containing prismatic precipitates exhibited a lower proportion of tension twins, with only approximately one-third of the twinning transfer observed compared with that with basal precipitates.

(2) The analysis of twinning crossover and variant behavior revealed that prismatic precipitates exhibited a more obvious hindering effect on twin growth compared with the basal precipitates.

(3) The calculation using the Orowan incremental model indicated that the reduced proportion of tension twins in the Mg−Sn alloy with prismatic Mg_2Sn could be ascribed to a larger critical resolved shear stress (CRSS) increment for tensile twins compared with basal precipitates.

(4) A evident reduction in twin transfer was observed in the Mg−Sn alloy with prismatic Mg_2Sn, attributed to hindering effects induced by higher GNDs and enhanced CRSS of tensile twins.

CRediT authorship contribution statement

Rui-hao FU: Methodology, Data curation, Visualization, Writing – Review & editing; **Yang-jie WAN:** Investigation, Formal analysis, Writing – Original draft; **Xun-fei XIONG:** Formal analysis; **Dong-di YIN:** Formal analysis; **Man-ping LIU:** Formal analysis, Data curation; **Bin JIANG:** Writing – Review & editing; **Zi-rong ZHOU:** Review & editing; **Yu-yang GAO:** Conceptualization, Funding acquisition, Validation; **Ying ZENG:** Methodology, Re-sources, Supervision, Funding acquisition, Writing – Review & editing.

Declaration of competing interest

The authors declare that they have no known competing financial interests or personal relationships that could have appeared to influence the work reported in this paper.

Acknowledgments

The authors gratefully acknowledge the National Natural Science Foundation of China (Nos. 52004227, U22A20187, 52201106), the China Postdoctoral Science Foundation (No. 2020M683240), and the Key Area Research and Development Program of Guangdong Province, China (No. 2020B090924002). We also thank the Analytical and Testing Center of Southwest Jiaotong University for assistance with EBSD, SEM and TEM experiments.

References

[1] HUANG X F, HUANG W G. Irrational crystallography of the $\langle 11\bar{2}0\rangle_{Mg}$ Mg_2Sn precipitates in an aged Mg−Sn−Mn alloy [J]. Materials Characterization, 2019, 151: 260−266.

[2] ZHONG L P, WANG Y J. Evolution of precipitate orientation and its effect on thermal conductivity of Mg−5Sn alloy [J]. Transactions of Nonferrous Metals Society of China, 2023, 33(6): 1701−1714.

[3] CHAI Y F, JIANG B, SONG J F,WANG Q H, GAO H, LIU B, HUANG G S, ZHANG D F, PAN F S. Improvement of mechanical properties and reduction of yield asymmetry of extruded Mg−Sn−Zn alloy through Ca addition [J]. Journal of Alloys and Compounds, 2019, 782: 1076−1086.

[4] XU C, ZHENG M Y, WU K, WANG E D, FAN G H, XU S W, KAMADO S, LIU X D, WANG G J, LV X Y. Effect of ageing treatment on the precipitation behaviour of Mg−Gd−Y−Zn−Zr alloy [J]. Journal of Alloys and Compounds, 2013, 550: 50−56.

[5] NIE J F. Effects of precipitate shape and orientation on dispersion strengthening in magnesium alloys [J]. Scripta Materialia, 2003, 48(8): 1009−1015.

[6] WAN Y J, ZENG Y, DOU Y C, HU D C, QIAN X Y, ZENG

Q, SUN K X, QUAN G F. Improved mechanical properties and strengthening mechanism with the altered precipitate orientation in magnesium alloys [J]. Journal of Magnesium and Alloys, 2022, 10(5): 1256−1267.

[7] LIANG M J, ZHENG J, LIU H, YAO B X. Microstructure and mechanical properties of AZ31 alloy prepared by cyclic expansion extrusion with asymmetrical extrusion cavity [J]. Transactions of Nonferrous Metals Society of China, 2022, 32(1): 122−133.

[8] NI R, MA S J, LONG L J, ZHENG J, ZHOU H, WANG Q D, YIN D D. Effects of precipitate on the slip activity and plastic heterogeneity of Mg−11Y−5Gd−2Zn−0.5Zr (wt.%) during room temperature compression [J]. Materials Science and Engineering A, 2021, 804: 140738.

[9] SASAKI T T, OH-ISHI K, OHKUBO T, HONO K. Enhanced age hardening response by the addition of Zn in Mg−Sn alloys [J]. Scripta Materialia, 2006, 55(3): 251−254.

[10] WAN Y J, ZENG Y, ZENG Q,SONG B, HUANG X F,QIAN X Y, JIANG B. Simultaneously improved strength and toughness of a Mg−Sn alloy through abundant prismatic lath-shaped precipitates [J]. Materials Science and Engineering A, 2021, 811: 141087.

[11] LIU F Y, XIN R L, WANG C P, SONG B, LIU Q. Regulating precipitate orientation in Mg−Al alloys by coupling twinning, aging and detwinning processes [J]. Scripta Materialia, 2019, 158: 131−135.

[12] GUO X Q, CHAPUIS A, WU P D, LIU Q, MAO X B. Experimental and numerical investigation of anisotropic and twinning behavior in Mg alloy under uniaxial tension [J]. Materials & Design, 2016, 98: 333−343.

[13] LIU F Y, XIN R L, ZHANG M X, PÉREZ-PRADO M T, LIU Q. Evaluating the orientation relationship of prismatic precipitates generated by detwinning in Mg alloys [J]. Acta Materialia, 2020, 195: 263−273.

[14] FAN H D, ZHU Y X, WANG Q, WANG Q Y. Effect of precipitate orientation on the twinning deformation in magnesium alloys [J]. Computational Materials Science, 2018, 155: 378−382.

[15] ROBSON J D, STANFORD N, BARNETT M R. Effect of precipitate shape and habit on mechanical asymmetry in magnesium alloys [J]. Metallurgical and Materials Transactions A, 2013, 44: 2984−2995.

[16] JIANG L, RADMILOVIĆ V R, SABISCH J E C, QI L, M.MINOR A M, C.CHRZAN D C, ASTA M. Twin nucleation from a single $\langle c+a\rangle$ dislocation in hexagonal close-packed crystals [J]. Acta Materialia, 2021, 202: 35−41.

[17] SU H, CHU Z B, XUE C, LI Y G, MA L F. Effect of initial texture on the $\{10\bar{1}2\}$ twinning variants selection mechanism in AZ31 magnesium alloy [J]. Materials Research Express, 2020, 7(8): 086503.

[18] XIN R L, GUO C F, JONAS J J, CHEN G, LIU Q. Variant selection of $\{10\bar{1}2\}$–$\{10\bar{1}2\}$ double twins during the tensile deformation of an AZ31 Mg alloy [J]. Materials Science and Engineering A, 2017, 700: 226−233.

[19] ZHOU B J, LI Y J, WANG L Y, JIA H L,ZENG X Q. The role of grain boundary plane in slip transfer during deformation of magnesium alloys [J]. Acta Materialia, 2022, 227: 117662.

[20] DENG J F, TIAN J, ZHOU Y C, CHANG Y Y, LIANG W, MA J Y. Plastic deformation mechanism and hardening mechanism of rolled Rare-Earth magnesium alloy thin sheet [J]. Materials & Design, 2022, 218: 110678.

[21] YIN D D, BOEHLERT C J, LONG L J, HUANG G H, ZHOU H, ZHENG J, WANG Q D . Tension-compression asymmetry and the underlying slip/twinning activity in extruded Mg−Y sheets [J]. International Journal of Plasticity, 2021, 136: 102878.

[22] NIESSEN F, NYYSSÖNEN T, GAZDER A A, HIELSCHER R. Parent grain reconstruction from partially or fully transformed microstructures in MTEX [J]. Journal of Applied Crystallography, 2022, 55: 180−194.

[23] DENG J F, TIAN J, CHANG Y Y, ZHOU Y C, LIANG W J, MA J Y. The role of $\{10\bar{1}2\}$ tensile twinning in plastic deformation and fracture prevention of magnesium alloys [J]. Materials Science and Engineering A, 2022, 853: 143678.

[24] KIM D H, MANUEL M V, EBRAHIMI F, TULENKO J, PHILLPOT S. Deformation processes in $[11\bar{2}0]$-textured nanocrystalline Mg by molecular dynamics simulation [J]. Acta Materialia, 2010, 58(19): 6217−6229.

[25] ZHANG Y F, MILLETT P C, TONKS M, BINER S B. Deformation twins in nanocrystalline body-centered cubic Mo as predicted by molecular dynamics simulations [J]. Acta Materialia, 2012, 60(18): 6421−6428.

[26] QU L, YANG Y, LU Y, FENG L, JU J H, GE P, ZHOU W, HAN D, PING D H. A detwinning process of $\{332\}\langle 113\rangle$ twins in beta titanium alloys [J]. Scripta Materialia, 2013, 69(5): 389−392.

[27] R.NIEZGODA S R, KANJARLA A K, BEYERLEIN I J, TOMÉ C N. Stochastic modeling of twin nucleation in polycrystals: An application in hexagonal close-packed metals [J]. International Journal of Plasticity, 2014, 56: 119−138.

[28] BARNETT M R, GHADERI A, QUINTA DA FONSECA J, ROBSON J D. Influence of orientation on twin nucleation and growth at low strains in a magnesium alloy [J]. Acta Materialia, 2014, 80: 380−391.

[29] GUAN D K, WYNNE B, GAO J H, HUANG Y H, RAINFERTH W M. Basal slip mediated tension twin variant selection in magnesium WE43 alloy [J]. Acta Materialia, 2019, 170: 1−14.

[30] GUO C F, XIN R L, DING C H, SONG B, LIU Q. Understanding of variant selection and twin patterns in compressed Mg alloy sheets via combined analysis of Schmid factor and strain compatibility factor [J]. Materials Science and Engineering A, 2014, 609: 92−101.

[31] HONG S G, PARK S H, LEE C S. Role of $\{10\bar{1}2\}$ twinning characteristics in the deformation behavior of a polycrystalline magnesium alloy [J]. Acta Materialia, 2010, 58(18): 5873−5885.

[32] XU C, FAN G H, NAKATA T, LIANG X, CHI Y Q, QIAO X G, CAO G J, ZHANG T T, HUANG M, MIAO K S, ZHENG M Y, KAMADO S, XIE H L. Deformation behavior of ultra-strong and ductile Mg−Gd−Y−Zn−Zr alloy with bimodal microstructure [J]. Metallurgical and Materials Transactions A, 2018, 49(5): 1931−1947.

[33] WANG B S, XIN R L, HUANG G J, LIU Q. Strain rate and texture effects on microstructural characteristics of Mg−3Al−

1Zn alloy during compression [J]. Scripta Materialia, 2012, 66(5): 239−242.
[34] ZHU Y L, LIU F Y, XIN R L, SONG B, LIU Q. Improving mechanical properties of an AZ91 alloy by properly combining aging treatment and torsion deformation [J]. Materials Science and Engineering A, 2020, 779: 139156.
[35] KANG Y H, HUANG Z H, WANG S C, YAN H, CHEN R S, HUANG J C. Effect of pre-deformation on microstructure and mechanical properties of WE43 magnesium alloy II: Aging at 250 and 300 °C [J]. Journal of Magnesium Alloys, 2020, 8(1): 103−110.
[36] WANG F L, J.BHATTACHARYYA J J, AGNEW S R. Effect of precipitate shape and orientation on Orowan strengthening of non-basal slip modes in hexagonal crystals, application to magnesium alloys [J]. Materials Science and Engineering A, 2016, 666: 114−122.
[37] ROBSON J D, STANFORD N, BARNETT M R. Effect of precipitate shape on slip and twinning in magnesium alloys [J]. Acta Materialia, 2011, 59(5): 1945−1956.
[38] DAVIS A E, ROBSON J D. Modelling magnesium alloys for improved isotropic and symmetric yield behaviour [C]// Magnesium Technology 2017. Cham: Springer, 2017: 303−311.
[39] DAVIS A E, ROBSON J D, TURSKI M. Reducing yield asymmetry and anisotropy in wrought magnesium alloys—A comparative study [J]. Materials Science and Engineering A, 2019, 744: 525−537.
[40] FULLMAN R L. Measurement of particle sizes in opaque bodies [J]. JOM, 1953, 5(3): 447−452.
[41] HIDALGO-MANRIQUE P, ROBSON J D, PÉREZ-PRADO M T. Precipitation strengthening and reversed yield stress asymmetry in Mg alloys containing rare-earth elements: A quantitative study [J]. Acta Materialia, 2017, 124: 456−467.
[42] NIE J F. Precipitation and hardening in magnesium alloys [J]. Metallurgical and Materials Transactions A, 2012, 43(11): 3891−3939.
[43] CHRISTIAN J W, MAHAJAN S. Deformation twinning [J]. Progress in materials science, 1995, 39(1/2): 1−157.
[44] SERRA A, POND R C, BACON D J. Computer simulation of the structure and mobility of twinning dislocations in hcp metals [J]. Acta Metallurgica et Materialia, 1991, 39(7): 1469−1480.
[45] GHAZISAEIDI M, HECTOR JR L G, CURTIN W A. First-principles core structures of ⟨*c*+*a*⟩ edge and screw dislocations in Mg [J]. Scripta Materialia, 2014, 75: 42−45.
[46] WANG B Z, TANG B, YOU C, WAN Y C, GAO Y H, CHEN Z Y, LU L W, LIU C M, WANG J. Dislocation arrays, precipitate bands and free zones in forged Mg−Gd−Y−Zr alloy [J]. Materials Science and Engineering A, 2020, 775: 138789.
[47] ZHANG S H, DENG L, TIAN W H, CHE L Z, LI Y. Deduction of a quadratic velocity field and its application to rolling force of extra-thick plate [J]. Computers & Mathematics with Applications, 2022, 109: 58−73.

含基面或柱面 Mg_2Sn 的 Mg−Sn 合金的压缩孪生行为

付瑞豪[1,2]，万杨杰[2]，熊训飞[2]，尹冬弟[2]，刘满平[3]，蒋 斌[1]，周梓荣[4]，高瑜阳[1]，曾 迎[1,2]

1. 重庆大学 国家镁合金材料工程技术研究中心，重庆 400044；
2. 西南交通大学 材料科学与工程学院 材料先进技术教育部重点实验室，成都 610031；
3. 江苏大学 材料科学与工程学院，镇江 212013；
4. 东莞理工学院 科技创新研究所，东莞 523007

摘 要：采用含有基面或柱面 Mg_2Sn 相的镁锡合金定量揭示析出取向对孪生行为的影响。对含有基面或柱面 Mg_2Sn 的 Mg−5%Sn(质量分数)合金进行压缩，研究其孪生行为。随后，构建一个 Orowan 强化模型，以定量研究孪生析出相的临界分切应力增量。结果表明，柱面析出相比基面析出相更能有效地阻碍拉伸孪晶的转移和生长。对比含基面析出相的合金，含柱面析出相的拉伸孪晶比例下降归因于拉伸孪晶的临界分切应力增量更大。含有柱面析出相的孪晶转移比率明显降低，归因于该合金中拉伸孪晶的几何必需位错较高和临界分切应力增强。值得注意的是，柱面析出相在压缩过程中对拉伸孪晶具有更好的阻碍作用。

关键词：镁锡合金；取向调控；孪生行为；Mg_2Sn 柱面相；Orowan 强化

(Edited by Xiang-qun LI)